Plant stiffness and biomass as drivers for drag forces under extreme wave loading: a flume study on mimics

Maike Paul[a,1,2], Franziska Rupprecht[b], Iris Möller[c], Tjeerd J Bouma[d], Tom Spencer[c], Matthias Kudella[a], Guido Wolters[e], Bregje K van Wesenbeeck[e], Kai Jensen[b], Martin Miranda-Lange[a], Stefan Schimmels[a]

[a] Forschungszentrum Küste (FZK), Merkurstr. 11, 30419 Hannover, Germany

[b] Applied Plant Ecology, Biocenter Klein Flottbek, University of Hamburg, Ohnhorststr. 18, 22609 Hamburg, Germany

[c] Cambridge Coastal Research Unit, Department of Geography, University of Cambridge, Downing Place, Cambridge CB2 3EN, UK

[d] Yerseke Spatial Ecology, Netherlands Institute for Sea Research (NIOZ), Korringaweg 7, 4401 NT, Yerseke, the Netherlands

[e] Deltares, Boussinesqweg 1, 2629 HV Delft, the Netherlands

[1] Present address: Institute of Geoecology, Technische Universität Braunschweig, Langer Kamp 19c, 38106 Braunschweig, Germany

[2] corresponding author, m.paul@tu-braunschweig.de

Abstract

Moving water exerts drag forces on vegetation. The susceptibility of vegetation to bending and breakage determines its flow resistance, and chances of survival, under hydrodynamic loading. To evaluate the role of individual vegetation parameters in this water-vegetation interaction, we conducted drag force measurements under a wide range of wave loadings in a large wave flume. Artificial vegetation elements were used to manipulate stiffness, frontal area in still water and material volume as a proxy for biomass. The aim was to compare: (i) identical volume but different still frontal area, (ii) identical stiffness but different still frontal area, and (iii) identical still frontal area but different volume.

Comparison of mimic arrangements showed that stiffness and the dynamic frontal area (i.e., frontal area resulting from bending which depends on stiffness and hydrodynamic forcing) determines drag forces. Only at low orbital-flow velocities did the still frontal area dominate the force-velocity relationship and it is hypothesised that no mimic bending took place under these conditions.

Mimic arrangements with identical stiffness but different overall material volume and still frontal area showed that forces do not increase linearly with increasing material volume and it is proposed that short distances between mimics cause their interaction and result in additional drag forces. A model, based on effective leaf length and characteristic plant width developed for unidirectional flow, performed well for the force time series under both regular and irregular waves. However, its uncertainty increased with increasing interaction of neighbouring mimics.

Key words

drag force, wave forcing, plant mimics, stiffness, biomass, frontal area

1. Introduction

It has been widely recognised that the interaction of flexible littoral vegetation (e.g. seagrass, salt marsh) with both oscillatory and unidirectional flow in shallow marine environments leads to a reduction of water velocity and hydrodynamic energy (Lightbody and Nepf, 2006; Möller et al., 1999; Yang et al., 2012). Moreover, recently Möller et al. (2014) showed that a transplanted salt marsh is even capable of substantial wave height reduction under simulated storm surge conditions. Given the increasing need for coastal protection, there is high interest in nature-based coastal defence. Using intertidal vegetation in such schemes is one of the most promising approaches to date (Barbier et al., 2008; Bouma et al., 2014; Temmerman et al., 2013). However, implementing such nature-based coastal defence schemes requires high quality modelling capability of flow and wave dissipation by vegetation fields, and hence a mechanistic understanding of vegetation-hydrodynamic interaction. The flow reducing capacity of vegetation is based on the drag the vegetation exerts on the flow (either unidirectional or oscillatory) which can be expressed by the drag coefficient C_D. In return, the vegetation canopy is exposed to these drag forces and its resistance to these determines its survival (Callaghan et al., 2007; Denny et al., 1998). Estimation of these forces has therefore received considerable attention from both the hydraulic (Chen et al., 2011; Henry and Myrhaug, 2013; Siniscalchi et al., 2012) and ecological (Carrington, 1990; Gaylord et al., 2003; Sand-Jensen, 2003) research communities.

The drag expressed by C_D can be used to estimate the rate of frictional dissipation which leads to the reduction of wave energy (Dalrymple et al., 1984). Several models have been developed to estimate C_D from wave and vegetation parameters (Dalrymple et al., 1984; Kobayashi et al., 1993; Maza et al., 2013; Méndez and Losada, 2004), expressed as a function of either the Reynolds number *Re* or the Keulegan-Carpenter number *KC* (see Henry et al. (2015) for a comprehensive review). These models have been applied to wave dissipation datasets from both field (Bradley and Houser, 2009; Paul and Amos, 2011) and laboratory studies (Augustin et al., 2009; Houser et al., 2015; Stratigaki et al., 2011) in low to medium energy wave conditions. Dissipation of waves with heights in excess of 20 cm in water depths greater than 1 m above a typical salt marsh canopy has so far only been measured by Möller et al. (2014) in a large wave flume, and by Yang et al. (2012) in the field. Möller et al. (2014) show that under high incident wave energy levels the structural integrity of the vegetation elements is exceeded and plant elements begin to fold and break, rather than flex and bend as they do in response to low to medium energy conditions. As vegetation response changes with changing hydrodynamic forcing, a drag coefficient which assumes plant rigidity can thus not necessarily be used to calculate the drag forces acting on the vegetation, particularly when extrapolating to extreme conditions (Bell, 1999). It is thus necessary to determine the drag forces acting on salt marsh vegetation directly, in order to assess its susceptibility to physical damage during storm surges. Only then will it be possible to properly assess vegetation resilience under such conditions.

Available direct measurements of drag forces on natural plants are scarce and, due to the restricted dimensions of most flumes, typically limited to small waves (wave height $H \leq 7$ cm) or low-velocity unidirectional flow (Bouma et al., 2005; Bouma et al., 2010). Laboratory measurements with two intertidal plant species (*Spartina anglica* and *Zostera noltii*) showed that under those relatively benign conditions, the drag forces decrease with decreasing stiffness and suggest that bending of the flexible plants causes this reduction (Bouma et al., 2005). This observation agrees well with other research undertaken on drag reduction and reconfiguration (Boller and Carrington, 2006; O'Hare et al., 2007; Siniscalchi and Nikora, 2012), indicating that the effective frontal area after reconfiguration is a major factor in explaining drag. On the other hand, systematic studies with both real (Bouma et al., 2010; Paul and Amos, 2011) and artificial (Paul et al., 2012) flexible coastal vegetation suggests that wave attenuation, and hence $C_{D,}$ in shallow water environments is governed by the amount of above ground standing biomass rather than by individual parameters such as leaf length or vegetation stiffness. This observation is also supported by a study on fresh water macrophytes (Penning et al., 2009).

According to theory, the drag force F acting on a plant, is related to the frontal surface area A which in return depends on vegetation stiffness (Aberle and Järvelä, 2013; Bouma et al., 2010). This relationship can be described as

$$F = \frac{1}{2}\rho C_D A u^{\beta} \qquad (1)$$

where ρ is density of water, u is water velocity and β is a tuning parameter which depends on the streamlining of the plant, typically <2 for flexible objects, and 2 for rigid objects (Vogel, 1994). Biomass is not explicitly included in this equation but biomass investments in stem material will typically be reflected in shoot stiffness and thus plant shape (Bouma et al., 2010). To account for reconfiguration in equation 1, the parameters C_D, A, β or a combination of these three have been used. Statzner et al. (2006) for instance propose to change C_D and/or A to account for plant reconfiguration, while Denny and Gaylord (2002) suggest the maximum projected area to be a constant A and to reflect shape changes in C_D and β. Luhar and Nepf (2011) have argued that plant posture, i.e. the flow-dependent position of the plant and all its components within the water, affects streamlining and frontal area and express this change through an 'effective leaf length'. They thus advocate constant C_D and β and propose *A* to be the product of a constant characteristic width and a variable effective leaf length. In addition to having only one variable parameter, the latter model has the advantage that all necessary parameters can be derived from material properties and flow measurements and do not require knowledge of plant posture. However, the model has so far only been validated under unidirectional flow.

From the existing data, it appears that vegetation stiffness (and resulting frontal area for any given applied force) and biomass are both key drivers in wave attenuation and associated drag forces. However, their respective relative importance in determining drag force and their potential interactions are not yet well understood. In order to unravel these relationships and improve the assessment of drag forces based on vegetation parameters, we conducted controlled experiments with plant mimics - in the form of flexible plastic strips - under a range of wave conditions. These strips were combined in such a way, that we maintained either (i) a constant frontal area, but with varying biomass (i.e., same number of strips but with different thickness; 8 x 1 mm strips vs. 8 x 2 mm strips), (ii) an identical biomass, but a contrasting frontal area (i.e., few thick strips or more thin strips to obtain a constant volume; 8 x 1 mm strips, 4 x 2 mm strips or 2 x 4 mm strips) or (iii) an identical stiffness between shoots, but a contrasting frontal area (i.e., contrasting numbers of identical strips; 4 x 2 mm strips vs. 8 x 2 mm strips). Moreover, we used the obtained data to evaluate whether or not the model based on effective leaf length (Luhar and Nepf, 2011) is also applicable to drag forces under the oscillatory motion of waves. Whilst we appreciate that coastal vegetation is often exposed to breaking waves in the swash zone, we limited our tests to non-breaking waves. This approach reduces the complexity of hydrodynamics, allowing us to focus on the effect of frontal area, biomass and stiffness of the vegetation elements. For the first time, the direct drag measurements in this study also covered wave loading under extreme events. The measurements reported here will, in particular, help improve existing drag models and, in general, inform future studies on vegetation resilience to high energy wave forcing.

2. Methods

Experiments were carried out in conjunction with tests of wave attenuation over natural salt marsh transplants (Möller et al., 2014). They were conducted in the 5 m wide, 7 m deep and approx. 310 m long Large Wave Flume (GWK) of the Forschungszentrum Küste (FZK) in Hannover, Germany.

2.1. Model setup

An elevated test section of 60 m length was constructed approx. 95 m from the wave paddle which raised the salt marsh and drag sensors 1.5 m above the flume floor. This was necessary to ensure sufficient water depth at the wave paddle to generate the desired waves and to allow waves to fully develop before reaching the test section. At the beginning of the test section, a concrete ramp with a slope of 1:1.7 for 1.2 m, followed by a slope of 1:10 over a distance of 7 m, was installed to allow for a smooth transition of waves (Figure 1a). Here waves shoaled, but did not break, before interacting with the strip arrangements for all treatments considered here. At the end of the test section, a gravel slope (1:10) was constructed for the same purpose. Wave breaking at the 1:6 asphalt slope at the end of the flume minimised wave reflection and active wave absorption of the wave maker was employed for the same purpose.

On the level test platform, 7.15 m away from the front edge, five drag sensors were deployed in a line normal to the direction of wave approach with the sensor heads flush with the flume floor. The drag sensors were installed 30 cm apart starting 106 cm from the flume wall (Figure 1b). They operated on the principle of a wheatstone bridge (Carrington, 1990; Denny, 1988) and measured forces in two directions up to 10 N (accuracy ±0.5% F.S., developed by Deltares). They were deployed to capture forces in the direction of, and counter to, wave propagation along the flume. An electromagnetic current meter (EMCM) was also deployed on the same cross-section, located 76 cm from the flume wall (Figure 1b). The EMCM was set to record point measurements at a height of 15 cm above the test platform. This height corresponds to half the height of mimic arrangements which were slightly set off the ground by the metal bar fitting (Figure 1c). It was chosen as a representative value for the bulk velocity acting on the arrangements for the non-uniform velocity profile under wave motion. Data from all instruments was collected simultaneously at a sampling rate of 100 Hz.

A range of wave conditions (wave heights of between 0.1 and 0.9 m and wave periods between 1.4 and 5.1 s) was applied in two different water depths (1 and 2 m above the test platform), using both regular and irregular waves. Irregular waves were generated with a JONSWAP spectrum (peak enhancement factor 3.3) over 1000 waves and then followed by a regular wave test run (n = 100 waves) with a wave height corresponding to the zeroth-moment wave height (H_{m0}) of the irregular test. Active wave absorption at the end of each test and sufficient waiting time ensured that all tests started with still water level. Not all tests yielded drag data, due to overloading of the sensors or instrument failure; these tests were excluded from the subsequent analysis.

2.2. Plant mimics

For the force measurements in the flume, plastic strips attached to the drag sensors were used as a simplified representation of vegetation, or vegetation mimic, with varying degrees of stiffness. While the strips do not represent a particular plant species, they enabled us to easily manipulate individual parameters and hence assess their effect on drag in a more controlled fashion than would have been possible with real plants. A horizontal metal bar was mounted on each drag sensor and oriented normal to the wave direction. On the metal bars of four drag sensors different sets of plastic strips were mounted (Figure 1c). The fifth drag sensor was fitted with the horizontal metal bar but without any of the plastic strips to allow recording of the drag forces exerted on the mounting-bar alone as an experimental control treatment. Strips were all cut from Lexaan plates (mass density 1240 kg m^{-3}) to a standard length and width of 25 cm and 0.55 cm respectively, but using plates of three different thicknesses (1, 2, and 4 mm). Lexaan was selected as it is a highly flexible type of plastic but shows a distinct difference in stiffness between the three material thicknesses chosen here. Thicknesses were chosen so as to ensure that all mimics had sufficient rigidity to make their movement stiffness-dominated rather than buoyancy-dominated (Luhar and Nepf, 2011) and were yet flexible enough to be considered non-rigid. By varying the material thickness (simulated 'stiffness') the bending behaviour and hence frontal area was varied while keeping the material properties identical for ease of comparison.

In addition, the number of strips per drag sensor was varied to achieve a range of different material volumes (simulated 'biomass') per drag sensor exposed to the same experimental conditions (Table 1). To characterise the material, its flexural rigidity was derived by a 3-point-bending test according to the methodology described by Rupprecht et al. (2015). A sample was placed horizontally across two supporting bars spaced 15 times the sample thickness and the centre was pushed down with a third bar. The force required to push the sample down a given distance was recorded and the slope of the force-distance relationship (P/h) was used to determine flexural rigidity (J):

$$J = \frac{\left(\frac{s}{2}\right)^3 P}{6h} \qquad (2)$$

where s is the distance between supporting bars (Paul et al., 2014).

2.3. Data processing

Horizontal orbital velocities were obtained from the EMCM time series. To eliminate noise from the signal, a Fast Fourier Transformation was conducted on the whole time series and a low pass filter (f_l = 0.7 Hz) applied. For regular wave tests, the data were re-transformed into the time domain and the first 11 fully developed waves were used for subsequent analysis (Figure 2a). This eliminated any effects caused by reflection from the end of the flume. Zero-upcrossing was used to identify individual waves from the horizontal component of the velocity data and determine maximum horizontal orbital velocity $u_{r,max}$ and period T_r for each wave. This data was then averaged to yield a single value for each test. Moreover, time series of the individual waves were averaged to obtain a representative wave velocity time series at 15 cm above the test platform. To reduce noise in the representative time series, the longest and shortest wave in each record were removed, resulting in n = 9 for averaging.

For the irregular wave tests, elimination of reflection and averaging were not possible and consequently the whole time series of fully developed waves was used for spectral analysis using Fast Fourier Transformation. An additional high pass filter ($f_p/2.1$, f_p = peak frequency) was applied and a representative horizontal orbital velocity ($u_{i,m0}$) (analogue to standard wave height analysis) computed

$$u_{i,m0} = 4\sqrt{\sum_{j=1}^{m} \mathrm{S(f)}_j \Delta\mathrm{f}} \qquad (3)$$

where m is the total number of frequency components, $S(f)$ is the velocity spectrum and Δf the frequency band width. Values refer to the measurement point 15 cm above the bed which corresponds to half the mimic arrangement height and is considered the location where the flow is representative of the bulk velocity acting on the mimics. Processing of time series for drag forces was done analogous to horizontal orbital velocities to obtain F_r for regular and F_{m0} for irregular wave tests. $\mathrm{F_{m0}}$ is the force derived from the 0th moment of the force spectrum $S_F(f)$ and hence a representative parameter to describe the force acting by the waves constituting the applied wave spectrum.

To remove the impact of the horizontal bar to which the mimics were attached (Figure 1c), control runs with the strip-free bar were processed first. Consecutively, a best fit for $F_{control} \sim u^2$ in correspondence with the Luhar and Nepf (2011) model was found for regular and irregular waves, respectively:

$$\mathrm{F_{r,control}} = 0.53\mathrm{u}|\mathrm{u}| \qquad (4)$$

$$\mathrm{F_{m0,control}} = 0.22\mathrm{u}|\mathrm{u}| \qquad (5)$$

From these relationships, control time series were computed for each test run and subtracted from the raw force time series for each mimic arrangement prior to processing according to the above protocol.

2.4. Modelling

To estimate mimic posture without knowledge of its bending angle, the buoyancy parameter *B* and the Cauchy number *Ca*, i.e. the two dimensionless parameters driving plant posture, were derived (Luhar and Nepf, 2011).

$$B = \frac{\Delta\rho g b t l^3}{J} \qquad (6)$$

$$Ca = \frac{1}{2}\frac{\rho C_D b u^2 l^3}{J} \qquad (7)$$

where $\Delta\rho$ is the difference in density between water and the mimic. As mentioned above, plant posture affects streamlining and thus frontal area. The latter can be expressed by the effective leaf length l_{eff} (Luhar and Nepf, 2011):

$$l_{eff} = \left(1 - \frac{(1-0.9Ca^{-1/3})}{1+Ca^{-3/2}(8+B^{3/2})}\right) l \qquad (8)$$

Substituting into eq. 1 and using $\beta = 2$ as proposed by Luhar and Nepf (2011) allows estimation of the drag forces for regular and irregular waves respectively, from velocity measurements:

$$F_{modelled} = \frac{1}{2}\rho C_D b l_{eff} u^2 \qquad (9)$$

with $C_D = 1.95$ for a rigid, upright blade (Vogel, 1994). To capture negative forces under the wave trough, u^2 was replaced by $u|u|$ in eq. 9. The model was applied to the averaged time series for regular waves based on the first 11 fully developed waves in the record and the full time series for irregular waves by substituting *u* in eq. 9 with $u_{r,max}$ and $u_{i,m0}$ obtained from the time series recorded 15 cm above the bed, respectively. This modelled time series was then processed analogous to the measured force time series to obtain $F_{r,model}$ and $F_{m0,model}$ respectively. The goodness-of-fit for the Luhar and Nepf (2011) model was assessed using linear regression in the averaged time series for regular, and the full time series for irregular, waves. All data pre-processing was done in L~davis (provided by FZK) and processing as well as statistical analysis was conducted in MATLAB®.

3. Results

Throughout all experimental conditions, the force recorded by the drag sensors with metal bars but without plastic strips was generally low ($F_r < 0.4$ N and $F_{m0} < 0.5$ N). However, at low velocities the strip mounting bars accounted for up to 19% of the measured forces for any strip arrangement at a given horizontal orbital velocity. The metal bar's influence was therefore removed from the force measurements during pre-processing.

3.1. Measured drag forces

Time series of forces and horizontal orbital velocities during regular and irregular wave tests showed that the forces changed direction in correspondence with the wave orbital cycle. However, forces were not necessarily in phase with the hydrodynamic loading (Figure 2b-e). No systematic response could be detected, with forces leading velocity in some cases (e.g. Figure 2b) and lagging velocity in others (e.g. Figure 2e). The phase lag may result from different bending behaviour of the mimics depending on their stiffness and the wave period. However, no video footage of the mimics was available to explore the link of these phase differences to mimic motion in detail.

For all strip arrangements, the acting forces increased with increasing horizontal orbital velocity, both for regular (Figure 3a) and irregular waves (Figure 3b). In both cases, the strip arrangement with the highest volume (8 x 2 mm) yielded forces that were on average 1.9 and 2.7 times higher than forces for the arrangements with half the volume (8 x 1 mm and 4 x 2 mm, respectively).

At low orbital velocities under regular waves ($u_{r,max} < 0.4$ m s^{-1}), frontal area appeared to influence drag forces, as the three arrangements with identical volume but different number of strips per arrangement (i.e. 8 x 1 mm, 4 x 2 mm and 2 x 4 mm) resulted in forces increasing with increasing number of strips per arrangement (Figure 3a). The forces recorded with the 8 x 1 mm and 4 x 2 mm arrangements exceeded those recorded with the 2 x 4 mm arrangement by a factor of 1.2 and 2.3 respectively. With increasing $u_{r,max}$ the difference between the 8 x 1 mm and 4 x 2 mm strip arrangement reduced and recorded forces became comparable in the velocity range 0.4 - 0.7 m s^{-1} when the standard deviations are considered. Beyond $u_{r,max} = 0.7$ m s^{-1}, forces on the 4 x 2 mm arrangement exceeded those for the 8 x 1 mm arrangement, while values for the 2 x 4 mm arrangement increased more rapidly with increasing velocities but still remained lower than for the other arrangements across the whole velocity range tested. Comparing the 4 x 2 mm and 8 x 2 mm arrangement for regular waves shows that material volume has an effect on drag forces, but that this effect is neither linear nor constant. At low velocities the 8 x 2 mm arrangement yielded more than three times the forces measured for the 4 x 2 mm arrangement (3.17 for $u_{r,max}$ = 0.2 m s^{-1}), while this difference decreased to a factor of 2.10 for $u_{r,max}$ = 0.59 m s^{-1}.

The influence of frontal area on drag forces at low velocities was also visible for irregular waves ($u_{i,m0}$ < 0.8 m s^{-1}). Similar to regular waves, the difference in forces measured with the 8 x 1 mm and 4 x 2 mm arrangement reduced with increasing $u_{i,m0}$ until they merged onto approx. one line for $u_{i,m0}$ > 1 m s^{-1} (Figure 3b). In contrast to the regular wave tests, however, forces observed with the 2 x 4 mm arrangement remained consistently a factor of approx. 2 lower than for the other arrangements with identical volume. Doubling the volume at constant material stiffness (i.e. from the 4 x 2 mm to 8 x 2 mm arrangement) led to an increase of drag forces by a factor of 2.06 - 2.81. In the same way as for regular waves, this factor decreased with increasing velocity.

Across all flow velocities tested, forces under irregular waves remained below those for corresponding regular wave tests (Figure 4). This can be attributed to the different computation methods used to derive statistical values from the measured force time series; F_r refers to the maximum force in the wave cycle, while F_{m0} is a statistical parameter describing the whole spectrum which includes all waves in the spectrum.

3.2. Modelled drag forces

Flexural rigidity (Table 1) was used to estimate the effective leaf length l_{eff} in order to apply the Luhar and Nepf (2011) model to the data. The model provided a very good fit (R^2 > 0.93) for the averaged force time series for most mimic arrangements in all regular wave tests (Figure 2b-e). Even in cases with deviations in the maximum and minimum forces in the wave cycle (Figure 2e), the model captured the overall shape of the force time series and also reproduced the reduced rate of change in forces during flow reversal. Comparing modelled and measured values for F_r over the whole velocity range tested showed a very good fit (Table 1), with a slight underprediction for mimics of 1 and 2 mm thickness. Forces recorded by the 2 x 4 mm arrangement were overpredicted at high velocities (Figure 4). The model indicated that forces for the 4 x 2 mm arrangement exceeded the ones for the 8 x 1 mm arrangement for $u_{r,max}$ > 0.47 m s^{-1}. Comparison of the modelled relationships showed that mimic thickness, and hence stiffness, affects forces in the low velocity ranges. The thicker, i.e. stiffer, the mimic is, the higher is the velocity at which the force-velocity relationship becomes approx. linear and the steeper the slope of this linear section becomes.

Similar to the pattern under regular waves, the model reproduced the time series of forces well for irregular wave tests. Scatter plots (Figure 5) show that high forces under wave crests were generally slightly underpredicted, while an overprediction of forces under wave troughs occurred in some cases (e.g. Figure 5d). Considering the F_{m0} values across the whole velocity range tested, the quality of model fit remained very good (Table 1, Figure 4), but showed a stronger underprediction for the 8 x 2 mm arrangement than for the 4 x 2 mm arrangement. These findings suggest that stiffness was not the driving parameter in this case as stiffness was identical for both arrangements. The model shows forces for the 4 x 2 mm arrangement to exceed the ones for the 8 x 1 mm arrangement for $u_{i,m0}$ > 1.28 m s^{-1} and, despite the model's tendency for underprediction, this agrees well with the measured data, where such a ratio first occurred at $u_{i,m0}$ > 1.26 m s^{-1} (Figure 3).

4. Discussion

In this study, vegetation mimic arrangements with different volume, stiffness and still frontal area were exposed to a wide range of wave forcing. Drag forces acting on the mimics were both measured directly and modelled using the concept of effective leaf length. The resulting model, initially developed under unidirectional flow, was applied to forces under oscillatory flow and performed well for regular as well as irregular waves. In addition, comparison of measurements and model revealed that plants within a patch may interact with each other in the cross-stream direction which can have strong implications for vegetation stability, sediment trapping and the characterisation of vegetated foreshores.

4.1. The effect of frontal area on drag forces

Under a given hydrodynamic forcing, the flexural rigidity determines l_{eff} which, under unidirectional flow, has been shown to be directly related to the drag force acting on the plant or mimic (Luhar and Nepf, 2011). This study applied the concept of effective leaf length and the resulting model to forces under oscillatory flow. Overall, the model performed well for time series and statistical parameters, i.e. F_r and F_{m0}, under both regular and irregular waves. The slight underprediction of forces may be due to the fact that the model was originally derived for unidirectional flow. The difference is likely to be caused by additional inertia forces which apply due to acceleration under waves (Denny et al., 1998); these forces increase with increasing horizontal orbital velocity. The data reflects this increase, as the model's goodness-of-fit reduces with increasing $u_{r,max}$ and $u_{i,m0}$ (Figure 4 and 5). However, in order to evaluate whether forces under waves are higher for the same flow velocity compared to unidirectional flow, comparative force measurements need to be conducted in the future. An additional aspect is that l_{eff} is by definition less than, or equal to, the physically deflected height as it accounts for streamlining in addition to the reduced frontal area due to bending (Luhar and Nepf, 2011). Streamlining may not apply to the mimics under waves and the use of the physically deflected height may be more appropriate in this case. At high velocities ($u_{r,max} > 0.77$ m s^{-1}), the live *Elymus athericus* plants were found to fold over at the base and streamline to a flat position for some time during the wave cycle (Möller et al., 2014). The similarity between *Elymus athericus* and the mimics in terms of their material properties suggest that their bending behaviour under the same hydrodynamic forcing may be similar as well. Furthermore, the data for regular waves suggest that mimic response changes with increasing velocities. At low ($u_{r,max} < 0.4$ m s^{-1}) velocities, mimic bending appears to be so low that all mimic arrangements remain fully upright. As a consequence, still frontal area at a constant material volume (i.e. mimic arrangements 8 x 1 mm, 4 x 2 mm and 2 x 4 mm) determines drag forces rather than flexural rigidity (Figure 3). At intermediate velocities (0.4 m s^{-1} < $u_{r,max}$ < 0.7 m s^{-1}) different bending angles of the 8 x 1 mm and 4 x 2 mm arrangement lead to similar l_{eff} and hence comparable drag forces.

Att $u_{r,max} > 0.7$ m s^{-1} different bending behaviour due to different mimic stiffness between all three arrangements leads to deviations in l_{eff} and hence no direct relationship between mimic properties and drag forces. To assess changes in deflected height with increasing orbital velocity and to evaluate the relationship of deflected height and l_{eff}, future work should include visual observations of the mimics' motion and bending angle.

4.2. The effect of stiffness on drag forces

The similar forces for the 8 x 1 mm and 4 x 2 mm arrangement with identical material volume at high velocities suggest that, in this exposure range, drag forces on vegetation depend on material volume (i.e. above ground standing biomass) rather than stiffness. This finding agrees with previous observations (Bouma et al., 2010; Paul and Amos, 2011; Penning et al., 2009), although it should be noted that these studies only covered a limited velocity range due to practical reasons. The results over the wider range of velocities presented here emphasise the fact that conclusions drawn from small datasets need to be evaluated with care and that extrapolation to other velocity ranges may not be possible (Bell, 1999). Considering the whole range of velocities tested here, material stiffness described by flexural rigidity J appears to play an important role in the force-velocity relationship across the whole velocity range as it determines the slope of this relationship (Figure 4). This observation agrees well with data obtained under unidirectional flow (Aberle and Järvelä, 2013; Callaghan et al., 2007). In regions with low wave forcing and hence low orbital velocities (i.e. a salt marsh high in the tidal frame) it may therefore be beneficial for a plant to produce thicker yet stiffer stems if this reduces the frontal area exposed to hydrodynamic forcing. Conversely, in regions with higher wave forcing (such as a pioneer salt marsh edge), vegetation viability may benefit from the presence of more flexible shoots with respect to drag forces, even if this increases the plant’s frontal area in still water. Such a gradient of stiffness with exposure to hydrodynamic forcing has been described by Rupprecht et al. (2015). They found an increase in Young's bending modulus from the low marsh species *Puccinellia maritima* (737-1995 MPa) to the high marsh species *Elymus athericus* (1952-4082 MPa).

4.3. The effect of material distribution on drag forces

When considering mimic arrangements with identical stiffness (i.e. 4 x 2 mm and 8 x 2 mm), an effect of material volume and frontal area on drag forces was observed (Figure 3). The fact that forces did not exactly double between the two mimic arrangements at a given velocity can potentially be attributed to the different distances between the individual model strips. The closer the strips are positioned together, the more they will influence each other through the turbulence generated at their edges (Sparboom et al., 2006) which is likely to lead to increased overall forces acting on the arrangement. This would also explain the reduced quality in model fit between the 8 x 2 mm and 4 x 2 mm arrangement (Figure 4b and d) as the model was developed for individual plants, making it unable to consider interactions between structures. To capture these effects of strip interaction and thus account for more complex plant geometries, computation of the characteristic width *b* would need to be modified. In this experiment, the model was applied by using the strip width to calculate the buoyancy parameter *B* and the Cauchy number *Ca*, while the product of strip width and number of strips was used in eq. 9 to compute the modelled force. This approach assumes a single solid strip and does not account for the effect of complex structures with gaps between individual elements. Consequently, the model in its current form predicts exactly twice the force for the 8 x 2 mm arrangement than for the 4 x 2 mm arrangement. Unfortunately, the used mimic arrangements did not allow for a more detailed parameterisation of the effective width. Systematic tests with defined gap sizes between strips are required to close this knowledge gap in the future.

The dependence of drag forces on cross-stream gap size indicates that forces acting on plants when positioned within a vegetation patch are more complex than previously suggested. Investigations of wave forces in patches of macroalgae have shown that individual specimens can reduce the forces acting on them by 'hiding' behind upstream organisms (Carrington, 1990; Eckman et al., 1994). Force measurements on rigid and flexible structures under unidirectional flow have demonstrated that both down-stream and cross-stream distance between structures affect acting forces (Schoneboom et al., 2010; Schoneboom et al., 2011), but that both distances are related to the wake flow structure of upstream elements in different array setups (offset vs. in line). The absence of upstream or downstream structures in this study suggests that neighbouring vegetation stems can be assumed to cause the observed patterns of enhanced drag forces when plants grow more closely spaced laterally. Consequently, a threshold vegetation spacing may exist below which the shading effect of upstream plants outweighs the additional forces from neighbouring stems. This threshold spacing would, however, depend upon wake evolution and therefore on vegetation diameter and complexity of shape as well as hydrodynamic forcing. Vegetation spacing is an important factor in marsh ecology, as marsh vegetation typically needs to surpass a density threshold for significant sediment accretion to occur (Bouma et al., 2009; Peralta et al., 2008). Hence we advocate further study of the effect of vegetation spacing on acting forces and sediment transport to enhance our knowledge both from a hydrodynamic as well as an ecological point of view.

5. Conclusions

In this study, we conducted direct force measurements on mimic arrangements representing vegetation elements of varying stiffness and material volume characteristics. All mimic arrangements were exposed to hydrodynamic forcing under regular and irregular waves, covering a wide range of conditions including high energy events.

The results confirm that vegetation stiffness, rather than biomass, is the driving parameter behind the force-velocity relationship as it is stiffness that determines bending and hence effective leaf length under hydrodynamic forcing. Under low forcing, forces are distributed according to the still frontal area of the mimic arrangement; this may be due to the lack of bending under these conditions. While under increased orbital velocities, the combination of characteristic width and bending can lead to the same response for mimic arrangements with identical material volume but different still frontal area.

Moreover, the observations of different mimic arrangements suggest that plants within a patch interact with each other in the cross-stream direction. If shoots grow close enough to each other, the turbulence at their edges will affect neighbouring plants and increases the drag force acting on them even if the plants are not in direct contact with each other.

The force measurements were also modelled, applying the model based on effective leaf length by Luhar and Nepf (2011) to orbital velocities. Overall, the model performed very well and was able to reproduce force time series for regular as well as irregular waves. However, it did not reproduce the force increase due to the interaction of neighbouring mimics which led to small deviations between modelled and measured data. In order to incorporate these interactions in the model and allow for its application to more complex plant shapes, visual observations alongside force measurements are now required for different mimic configurations. Such work would further develop existing models, improve characterisation of vegetated foreshores and aid better design of soft engineering interventions on low-lying sedimentary shorelines.

Acknowledgements

We thank all of the staff at the Grosser Wellenkanal as well as B. Evans, J. Tempest, K. Milonidis and C. Edwards, Cambridge University, and D. Schulze, Hamburg University, for their invaluable logistical assistance. Our gratitude also goes to two anonymous reviewers whose comments greatly helped to improve the manuscript. The work described in this publication was supported by the European Community's 7th Framework Programme through the grant to the budget of the Integrating Activity HYDRALAB IV, Contract no. 261529 and a grant from The Isaac Newton Trust, Trinity College, Cambridge. M. Paul acknowledges funding by the German Science Foundation (grant no. PA 2547/1-1).

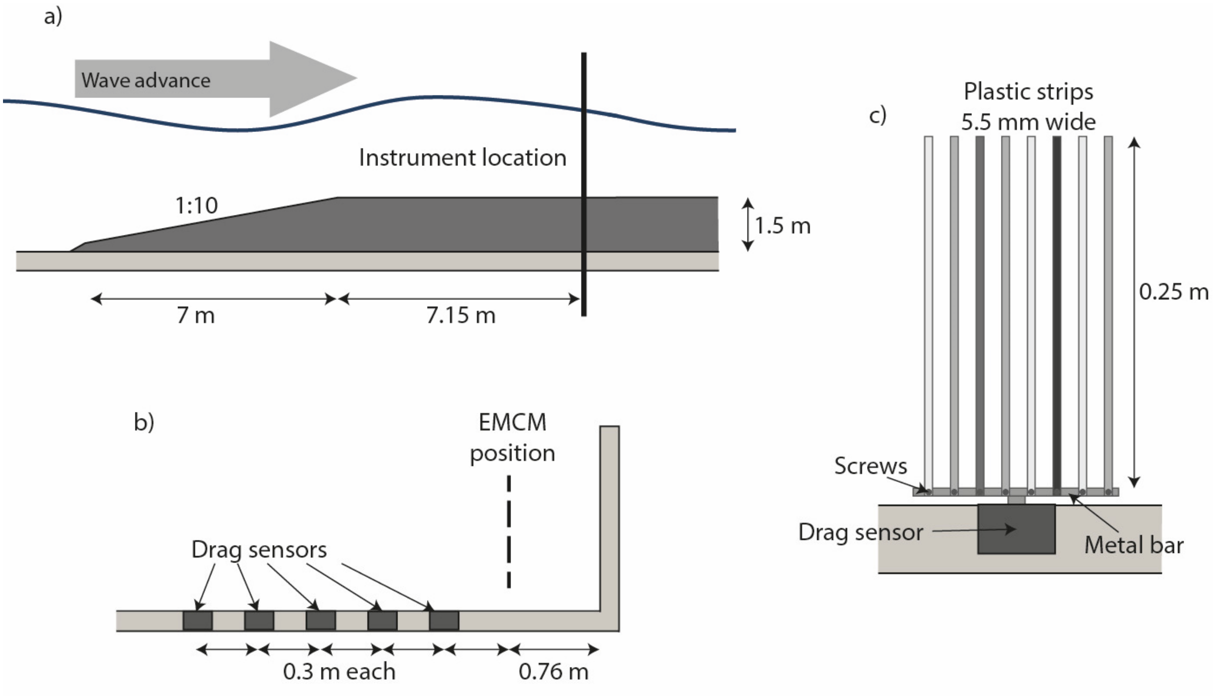

Figure 1: Schematic of instrument setup indicating a) the instrument location in a flume side view, b) a downstream view of the instrument location, and c) the mounting of strip arrangements on the drag sensors. At the black position a strip was attached for all arrangements. In addition, the dark shaded position was used for the 2 x 4 mm arrangement, for the 4 x 2 mm arrangement the medium shaded positions were used and the 8 x 2 mm and 8 x 1 mm arrangements used all positions.

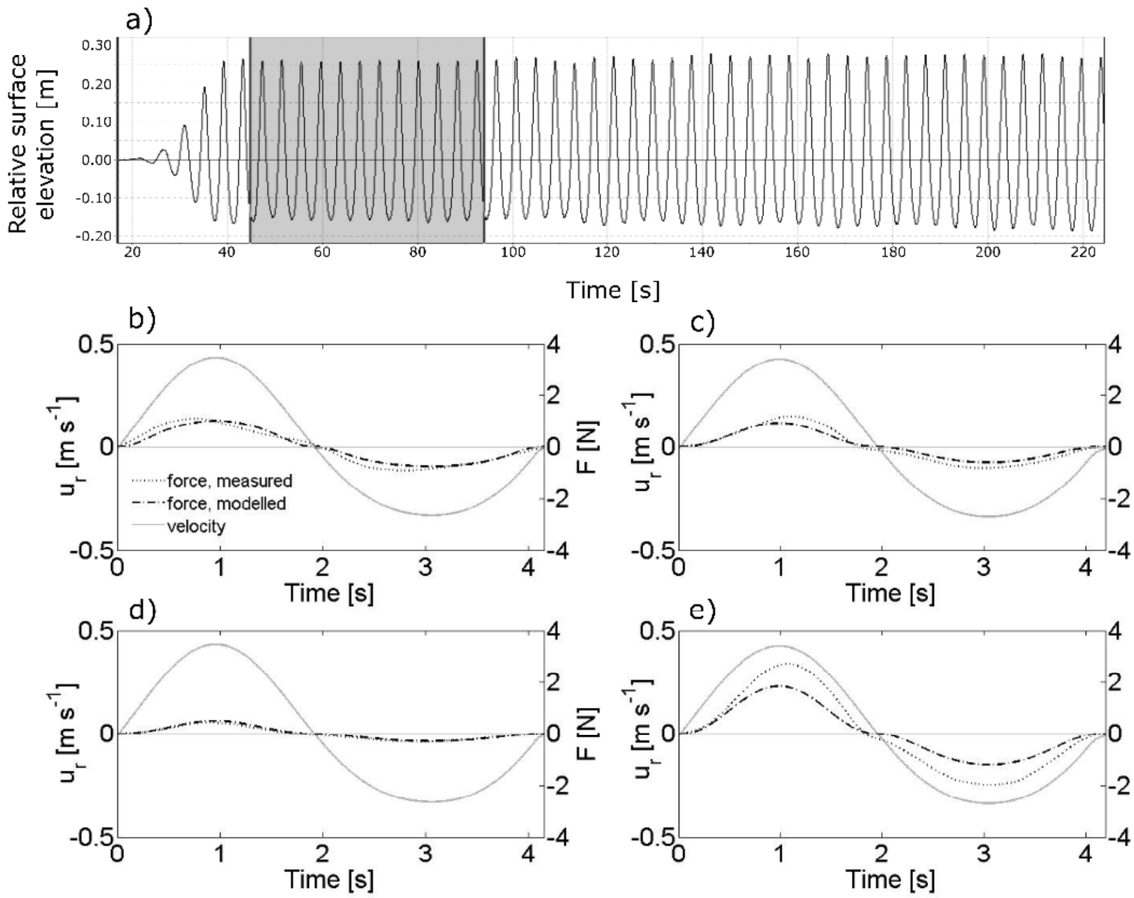

Figure 2: Time series of relative surface elevation under regular waves (*H* = 0.4 m, *T* = 4.1 s) in 2 m water depth with the grey shaded area indicating the first 11 fully developed waves used for analysis (a) and time series of averaged horizontal velocity and drag forces under the same conditions for b) the 8 x 1 mm arrangement (R^2 = 0.97, RMSE = 0.11, absolute maximum residual = 0.30), c) the 4 x 2 mm arrangement (R^2 = 0.95, RMSE = 0.11, absolute maximum residual = 0.49), d) the 2 x 4 mm arrangement (R^2 = 0.92, RMSE = 0.07, absolute maximum residual = 0.21), and e) 8 x 2 mm arrangement (R^2 = 0.96, RMSE = 0.21, absolute maximum residual = 0.68). R^2 gives the linear regression fit between measured and modelled force time series and RMSE is the root-mean-square error of this fit. These are illustrative examples; all other tests showed the same quality of model fit.

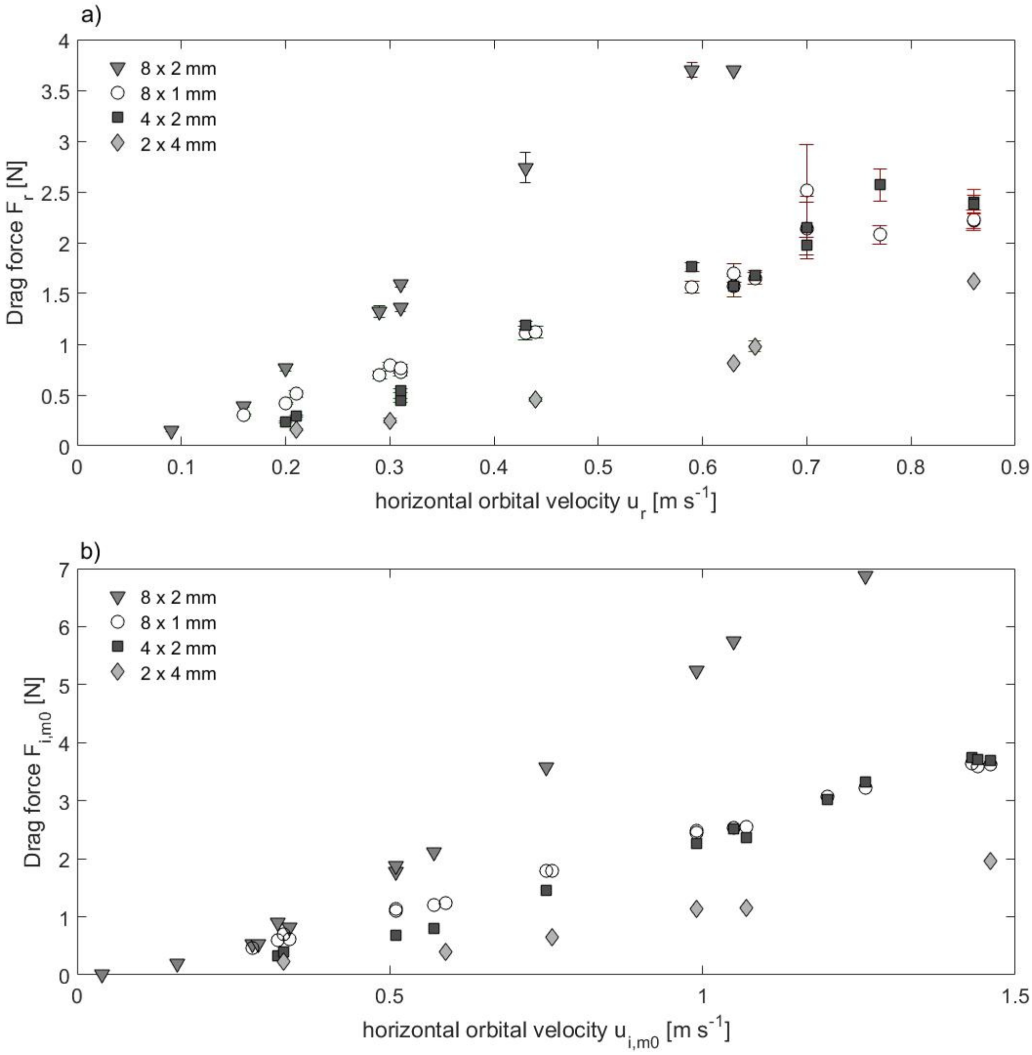

Figure 3: Drag forces for the different mimic arrangements in relationship to a) maximum horizontal orbital velocity $u_{r,max}$ for regular waves, b) horizontal orbital velocity $u_{i,m0}$ for irregular waves. For regular waves values are given with ± one standard deviation. Values for mimic arrangements are corrected for the influence of the horizontal metal bar.

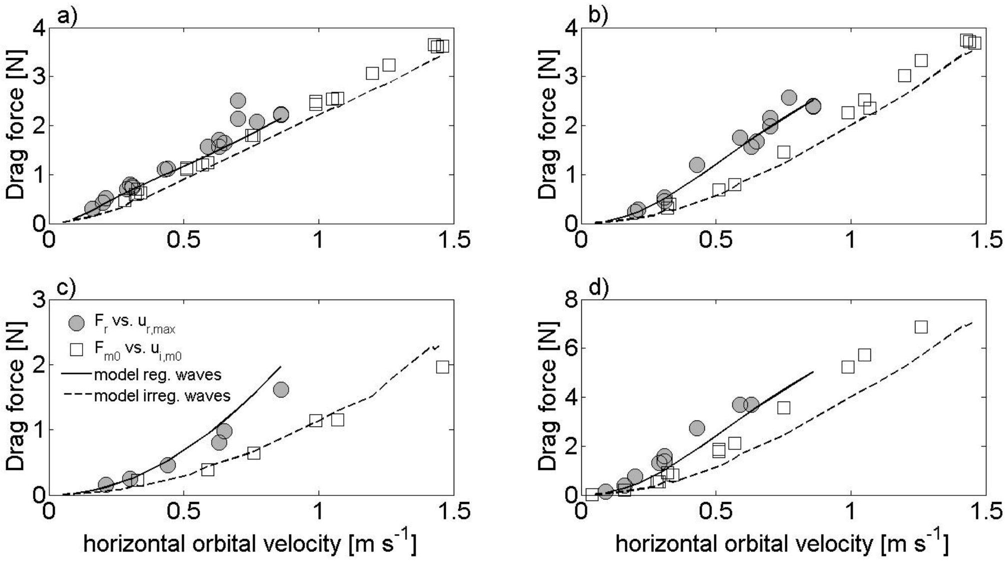

Figure 4: Measured drag forces and the fitted Luhar and Nepf (2011) model for the different mimic arrangements a) 8 x 1 mm, b) 4 x 2 mm, c) 2 x 4 mm, and d) 8 x 2 mm in relationship to horizontal orbital velocity 15 cm above the bed for regular and irregular waves. Standard deviation for the regular wave data is omitted for clarity.

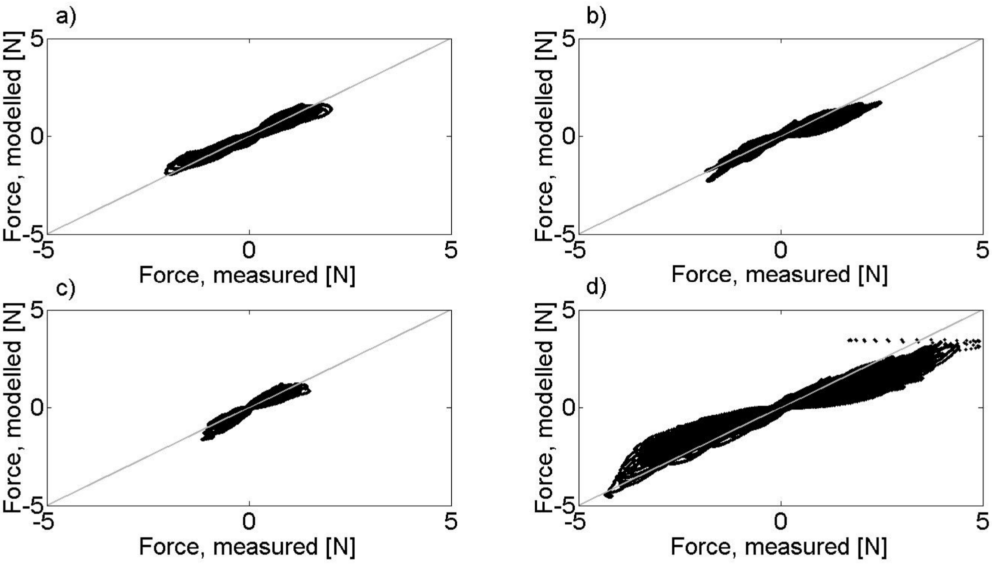

Figure 5: Scatter plot of the modelled forces vs. measured forces for irregular waves (H_{m0} = 0.4 m, T_p = 4.13 s) in 2 m water depth. The grey line depicts $F_{modelled} = a*F_{measured}$ with a = 1. For each dataset, a was computed using linear regression for a) the 8 x 1 mm arrangement (a = 0.85, R^2 = 0.94, RMSE = 0.09, absolute maximum residual = 0.54), b) the 4 x 2 mm arrangement (a = 0.80, R^2 = 0.91, RMSE = 0.09, absolute maximum residual = 0.88), c) the 2 x 4 mm arrangement (a = 0.96, R^2 = 0.86, RMSE = 0.06, absolute maximum residual = 0.65), and d) the 8 x 2 mm arrangement (a = 0.66, R^2 = 0.92, RMSE = 0.18, absolute maximum residual = 2.35). R^2 gives the linear regression fit between measured and modelled force time series and RMSE is the root-mean-square error of this fit.

Table 1: Parameters of the used mimic arrangements and goodness-of-fit parameters for the Luhar and Nepf (2011) model. Flexural rigidity is given ± standard deviation. The fit parameters refer to the relationship $F_{modelled} = a*F_{measured}$ for F_r and F_{m0} respectively across the whole velocity range tested, for the data shown in Figure 4.

Arrangement	Number of strips	Strip thickness (mm)	Still frontal area (cm^2)	Material volume (cm^3)	Flexural rigidity (Nm^2)	Fit parameter $a_{regular}$/ R^2	Fit parameter $a_{irregular}$/ R^2
8 x 1 mm	8	1	110	11	$1.36*10^{-3} \pm 3.73*10^{-5}$ (n = 9)	0.88/ 0.94	0.91/ 0.99
4 x 2 mm	4	2	55	11	$8.97*10^{-3} \pm 6.73*10^{-5}$ (n = 10)	0.97/ 0.96	0.91/ 0.99
2 x 4 mm	2	4	27.5	11	$6.57*10^{-2} \pm 3.21*10^{-3}$ (n = 10)	1.21/ 0.99	1.12/ 0.98
8 x 2 mm	8	2	110	22	$8.97*10^{-3} \pm 6.73*10^{-5}$ (n = 10)	0.82/ 0.96	0.77/ 0.99

References

Aberle, J., Järvelä, J., 2013. Flow resistance of emergent rigid and flexible floodplain vegetation. Journal of Hydraulic Research 51 (1), 33–45. doi:10.1080/00221686.2012.754795.

Augustin, L.N., Irish, J.L., Lynett, P., 2009. Laboratory and numerical studies of wave damping by emergent and near-emergent wetland vegetation. Coastal Engineering 56, 332–340. doi:10.1016/j.coastaleng.2008.09.004.

Barbier, E.B., Koch, E.W., Silliman, B.R., Hacker, S.D., Wolanski, E., Primavera, J.H., Granek, E.F., Polansky, S., Aswani, S., Cramer, L.A., Stoms, D.M., Kennedy, C.J., Bael, D., Kappel, C.V., Perillo, G.M.E., Reed, D.J., 2008. Coastal Ecosystem - Based Management with Nonlinear Ecologial Functions and Values. Science 319. doi:10.1126/science.1150349.

Bell, E.C., 1999. Applying flow tank measurements to the surf zone: predicting dislodgement of the Gigartinaceae. Phycological Research 47, 159–166.

Boller, M.L., Carrington, E., 2006. The hydrodynamic effects of shape and size change during reconfiguration of a flexible macroalga. Journal of Experimental Biology 209 (10), 1894–1903. doi:10.1242/jeb.02225.

Bouma, T.J., de Vries, M.B., Herman, P.M.J., 2010. Comparing ecosystem engineering efficiency of 2 plant species with contrasting growth strategies. Ecology 91 (9), 2696–2704. doi:10.1890/09-0690.1.

Bouma, T.J., de Vries, M.B., Low, E., Peralta, G., Tánczos, I.C., van de Koppel, J., Herman, P.M.J., 2005. Trade-offs related to ecosystem engineering: A case study on stiffness of emerging macrophytes. Ecology 86 (8), 2187–2199. doi:10.1890/04-1588.

Bouma, T.J., Friedrichs, M., van Wesenbeeck, B.K., Temmerman, S., Graf, G., Herman, P.M.J., 2009. Density-dependent linkage of scale-dependent feedbacks: a flume study on the intertidal macrophyte Spartina anglica. Oikos 118 (2), 260–268. doi:10.1111/j.1600-0706.2008.16892.x.

Bouma, T.J., van Belzen, J., Balke, T., Zhu, Z., Airoldi, L., Blight, A.J., Davies, A.J., Galván, C., Hawkins, S.J., Hoggart, S.P., Lara, J.L., Losada, I.J., Maza, M., Ondiviela, B., Skov, M.W., Strain, E.M., Thompson, R.C., Yang, S., Zanuttigh, B., Zhang, L., Herman, P.M.J., 2014. Identifying knowledge gaps hampering application of intertidal habitats in coastal protection: Opportunities & steps to take. Coastal Engineering 87, 147–157. doi:10.1016/j.coastaleng.2013.11.014.

Bradley, K., Houser, C., 2009. Relative velocity of seagrass blades: Implications for wave attenuation in low-energy environments. J. Geophys. Res. 114 (F01004), 1–13. doi:10.1029/2007JF000951.

Callaghan, F.M., Cooper, G.G., Nikora, V.I., Lamouroux, N., Statzner, B., Sagnes, P., Radford, J., Malet, E., Biggs, B.J., 2007. A submersible device for measuring drag forces on aquatic plants and other organisms. New Zealand Journal of Marine and Freshwater Research 41 (1), 119–127. doi:10.1080/00288330709509900.

Carrington, E., 1990. Drag and Dislodgment of an Intertidal Macroalga - Consequences of Morphological Variation in Mastocarpus-Papillatus Kutzing. Journal of Experimental Marine Biology and Ecology 139 (3), 185–200. doi:10.1016/0022-0981(90)90146-4.

Chen, L., Stone, M.C., Acharya, K., Steinhaus, K.A., 2011. Mechanical analysis for emergent vegetation in flowing fluids. Journal of Hydraulic Research 49 (6), 766–774. doi:10.1080/00221686.2011.621359.

Dalrymple, R.A., Kirby, J.T., Hwang, P.A., 1984. Wave diffraction due to areas of energy dissipation. J. Wtrwy., Port, Coast., and Oc. Engrg. 110 (1), 67–79. doi:10.1061/(ASCE)0733-950X(1984)110:1(67).

Denny, M.W., 1988. Biology and the mechanics of the wave swept environment. Princeton University Press, Princeton, New Jersey.

Denny, M.W., Gaylord, B., 2002. The mechanics of wave-swept algae. Journal of Experimental Biology 205 (10), 1355–1362.

Denny, M.W., Gaylord, B., Helmuth, B., Daniel, T., 1998. The menace of momentum: Dynamic forces on flexible organisms. Limnol. Oceangr 43 (5), 955–968. doi:10.4319/lo.1998.43.5.0955.

Eckman, J., Werner, F.E., Gross, T.F., 1994. Modelling some effects of behavior on larval settlement in a turbulent boundary layer. Deep-Sea Research 41 (1), 185–208. doi:10.1016/0967-0645(94)90067-1.

Gaylord, B., Denny, M.W., 1997. Flow and flexibility: I. Effects of size, shape and stiffness in determining wave forces on the stipitate kelps Eisenia arborea and Pterygophora californica. Journal of Experimental Biology 200, 3141–3164.

Gaylord, B., Denny, M.W., Koehl, M.A.R., 2003. Modulation of wave forces on kelp canopies by alongshore currents. Limnol. Oceangr 48 (2), 860–871. doi:10.4319/lo.2003.48.2.0860.

Henry, P.-Y.T., 2014. Bending properties of a macroalga: Adaptation of Peirce's cantilever test for in situ measurements of Laminaria digitata (Laminariaceae). American Journal of Botany 101 (6), 1050–1055. doi:10.3732/ajb.1400163.

Henry, P.-Y.T., Myrhaug, D., 2013. Wave-induced drag force on vegetation under shoaling random waves. Coastal Engineering 78, 13–20. doi:10.1016/j.coastaleng.2013.03.004.

Henry, P.-Y.T., Myrhaug, D., Aberle, J., 2015. Drag forces on aquatic plants in nonlinear random waves plus current. Estuarine, Coastal and Shelf Science 165, 10–24. doi:10.1016/j.ecss.2015.08.021.

Houser, C., Trimble, S., Morales, B., 2015. Influence of Blade Flexibility on the Drag Coefficient of Aquatic Vegetation. Estuaries and Coasts 38 (2), 569–577. doi:10.1007/s12237-014-9840-3.

Lightbody, A.F., Nepf, H.M., 2006. Prediction of velocity profiles and longitudinal dispersion in emergent salt marsh vegetation. Limnol. Oceangr 51 (1), 218–228. doi:10.4319/lo.2006.51.1.0218.

Luhar, M., Nepf, H.M., 2011. Flow-induced reconfiguration of buoyant and flexible aquatic vegetation. Limnol. Oceangr 56 (6), 2003–2017. doi:10.4319/lo.2011.56.6.2003.

Maza, M., Lara, J.L., Losada, I.J., 2013. A coupled model of submerged vegetation under oscillatory flow using Navier–Stokes equations. Coastal Engineering 80, 16–34. doi:10.1016/j.coastaleng.2013.04.009.

Méndez, F.J., Losada, I.J., 2004. An empirical model to estimate the propagation of random breaking and nonbreaking waves over vegetation fields. Coastal Engineering 51 (2), 103–118. doi:10.1016/j.coasaleng.2003.11.003.

Möller, I., Kudella, M., Rupprecht, F., Spencer, T., Paul, M., van Wesenbeeck, B.K., Wolters, G., Jensen, K., Bouma, T.J., Miranda-Lange, M., Schimmels, S., 2014. Wave attenuation over coastal salt marshes under storm surge conditions. Nature Geosci 7 (10), 727–731. doi:10.1038/ngeo2251.

Möller, I., Spencer, T., French, J.R., Leggett, D.J., Dixon, M., 1999. Wave transformation over salt marshes: a field and numerical modelling study from North Norfolk, England. Estuarine, Coastal and Shelf Science 49, 411–426. doi:10.1006/ecss.1999.0509.

Mullarney, J.C., Henderson, S.M., 2010. Wave-forced motion of submerged single-stem vegetation. Journal of Geophysical Research - Oceans 115 (C12061), 1–14. doi:10.1029/2010JC006448.

O'Hare, M.T., Hutchinson, K.A., Clarke, R.T., 2007. The drag and reconfiguration experienced by five macrophytes from a lowland river. Aquatic Botany 86 (3), 253–259. doi:10.1016/j.aquabot.2006.11.004.

Paul, M., Amos, C.L., 2011. Spatial and seasonal variation in wave attenuation over Zostera noltii. J. Geophys. Res. 116, C08019. doi:10.1029/2010JC006797.

Paul, M., Bouma, T.J., Amos, C.L., 2012. Wave attenuation by submerged vegetation: combining the effect of organism traits and tidal current. Mar. Ecol. Prog. Ser. 444, 31–41. doi:10.3354/meps09489.

Penning, W.E., Raghuraj, R., Mynett, A., 2009. The effect of macrophyte morphology and patch density on wave attenuation, in: Proceedings of 7th ISE and 8th HIC, Chile.

Peralta, G., van Duren, L.A., Morris, E.P., Bouma, T.J., 2008. Consequences of shoot density and stiffness for ecosystem engineering by benthic macrophytes in flow dominated areas: a hydrodynamic flume study. Mar. Ecol. Prog. Ser. 368, 103–115.

Ravenell, J., Seixas, A., Rosenthal, D.M., Williams, O., Ogedegbe, C., Sevick, M.A., Newsome, V., Jean-Louis, G., 2016. Effect of birthplace on cardiometabolic risk among blacks in the Metabolic Syndrome Outcome Study (MetSO). Diabetology & metabolic syndrome 8, 14. doi:10.1061/(ASCE)0733-950X(1993)119:1(30).

Rupprecht, F., Möller, I., Evans, B., Spencer, T., Jensen, K., 2015. Biophysical properties of salt marsh canopies — Quantifying plant stem flexibility and above ground biomass. Coastal Engineering 100, 48–57. doi:10.1016/j.coastaleng.2015.03.009.

Sand-Jensen, K., 2003. Drag and reconfiguration of freshwater macrophytes. Freshwater Biol 48 (2), 271–283. doi:10.1046/j.1365-2427.2003.00998.x.

Schoneboom, T., Aberle, J., Dittrich, A., 2010. Hydraulic resistance of vegetated flows: Contribution of bed shear stress and vegetative drag to total hydraulic resistance, in: Proceedings of the International Conference on Fluvial Hydraulics River Flow 2010. River Flow 2010, Braunschweig, Germany, pp. 269–276.

Schoneboom, T., Aberle, J., Dittrich, A., 2011. Spatial Variability, Mean Drag Forces, and Drag Coefficients in an Array of Rigid Cylinders, in: Rowinski, P. (Ed.), Experimental Methods in Hydraulic Research, vol. 1. Springer Berlin Heidelberg, Berlin, Heidelberg, pp. 255–265.

Siniscalchi, F., Nikora, V.I., 2012. Flow-plant interactions in open-channel flows: A comparative analysis of five freshwater plant species. Water Resour. Res. 48 (5). doi:10.1029/2011WR011557.

Siniscalchi, F., Nikora, V.I., Aberle, J., 2012. Plant patch hydrodynamics in streams: Mean flow, turbulence, and drag forces. Water Resour. Res. 48 (1). doi:10.1029/2011WR011050.

Sparboom, U., Hildebrandt, A., Oumeraci, H., 2006. Group interaction effects of slender cylinders under wave attack, in: Proceedings 30th International Conference on Coastal Engineering (ICCE), San Diego, USA, pp. 4430–4442.

Statzner, B., Lamouroux, N., Nikora, V.I., Sagnes, P., 2006. The debate about drag and reconfiguration of freshwater macrophytes: comparing results obtained by three recently discussed approaches. Freshwater Biol 51 (11), 2173–2183. doi:10.1111/j.1365-2427.2006.01636.x.

Stratigaki, V., Manca, E., Prinos, P., Losada, I.J., Lara, J.L., Sclavo, M., Amos, C.L., Cáceres, I., Sánchez-Arcilla, A., 2011. Large-scale experiments on wave propagation over Posidonia oceanica. Journal of Hydraulic Research 49 (sup1), 31–43. doi:10.1080/00221686.2011.583388.

Temmerman, S., Meire, P., Bouma, T.J., Herman, P.M.J., Ysebaert, T., De Vriend, Huib J., 2013. Ecosystem-based coastal defence in the face of global change. Nature 504 (7478), 79–83. doi:10.1038/nature12859.

Vogel, S., 1994. Life in moving fluids: the physical biology of flow, 2nd ed. Princeton University Press, Princeton, N.J.

Yang, S.L., Shi, B.W., Bouma, T.J., Ysebaert, T., Luo, X.X., 2012. Wave Attenuation at a Salt Marsh Margin: A Case Study of an Exposed Coast on the Yangtze Estuary. Estuaries and Coasts 35 (1), 169–182. doi:10.1007/s12237-011-9424-4.